

Crystal structure, lattice dynamics and superexchange in $M\text{AgF}_3$ 1D antiferromagnets ($M = \text{K}, \text{Rb}, \text{Cs}$) and $\text{Rb}_3\text{Ag}_2\text{F}_7$ Ruddlesden-Popper phase

Kacper Koterak,^{1*} Jakub Gawraczyński,¹ Gašper Tavčar,² Zoran Mazej,² Wojciech Grochala¹

¹ Centre of New Technologies, University of Warsaw, S. Banacha 2C, 02-097 Warsaw, Poland

² Jožef Stefan Institute, Jamova cesta 39, 1000 Ljubljana, Slovenia

Dedicated to Prof. M. Niezgodka at his 70th birthday

Keywords: theoretical modelling, silver fluorides, infrared spectra, Raman spectra, low dimensional materials

*e-mail: k.koterak@cent.uw.edu.pl

Abstract

With the use of lattice dynamics calculation within hybrid HSE06 framework we were able to understand vibrational spectra of $M\text{AgF}_3$ ($M = \text{K}, \text{Rb}, \text{Cs}$) compounds. Comparative theoretical study uncovered lack of monotonicity in calculated optical phonons associated with Ag-F stretching modes which can be explained through an interplay of Lewis acidity of M(I) cation and its size. We confirm the tetragonal unit cells of $M\text{AgF}_3$ ($M=\text{Rb}, \text{Cs}$) at room temperature. We also theoretically predict an orthorhombic RbAgF_3 polymorph as a ground state at low temperature. However, we were not able to detect it by the means of low temperature PXRD (at 80 K) nor low temperature Raman (at 154 K) due to a number of constraints. We also describe a novel Ruddlesden-Popper phase of $\text{Rb}_3\text{Ag}_2\text{F}_7$ which can be regarded as quasi-0D system, where superexchange coupling constant between the nearest Ag(II) centres reaches an impressive value of -240.2 meV.

1. Introduction

Systems composed of silver(II) and fluorine are in many ways exceptional.¹ Silver(II) is so reactive that fluorine is the only element, which may form thermodynamically stable compounds with it. The binary AgF_2 , on its own right, hosts many exciting phenomena such as strong mixing of Ag(d) and F(p) states,² appreciable magnetic superexchange in 2D,¹ remarkable covalence of Ag-F bonds³ and electronic structure at the verge of valence instability.³ These features render AgF_2 similar to copper(II) oxides and BaBiO_3 , which are precursors of two important families of superconductors. Said similarity places Ag(II) fluorides in the focus of solid state chemistry, physics and materials science. Introducing the third element to the chemical composition further broadens the playground and provides us with a multitude of interesting physical phenomena to be studied.⁴⁻⁶ The simplest modifications of AgF_2 are exemplified by ternary fluoroargentates(II), $M(\text{I})\text{AgF}_3$ and $M(\text{I})_2\text{AgF}_4$. While $M_2\text{AgF}_4$ systems have already been thoroughly studied,⁷⁻⁹ the $M\text{AgF}_3$ ones (particularly $M = \text{Rb}$ and Cs) remain explored unsatisfactorily.

Alkaline ternary fluoroargentates(II) of a general formula $M\text{AgF}_3$ ($M = \text{K}, \text{Rb}, \text{Cs}$) adopt a distorted perovskite structure, with alkaline atom substantially impacting level of distortion (Figure 1). Generally, smaller the alkali metal cation, the more distant from ideal cubic lattice is the resulting structure. The early study of these compounds was conducted half a century ago, when quality of laboratory X-ray sources was much worse than nowadays. An orthorhombic ($Pnma$) structure was then assigned to KAgF_3 and tetragonal ($I4/mcm$) ones to RbAgF_3 and CsAgF_3 (based on Guinier pattern analysis).¹⁰ Although data quality and purity of the samples were far from good, these are the only structures of RbAgF_3 and CsAgF_3 reported so far. Only in 2013, it was possible to substantially improve purity of KAgF_3 specimen, which permitted more sophisticated analyses to be conducted.¹¹ However, syntheses of RbAgF_3 and CsAgF_3 have not yet been improved. There is even less research regarding other alkali fluoroargentates(II). NaAgF_3 is proposed to be a monoclinic or triclinic NaCuF_3 -related post perovskite¹² while LiAgF_3 has not been prepared despite many attempts.¹³

The more recent study of KAgF_3 has showed that this compound exhibits a structural phase transition at 230 K which is of order/disorder type. The low-temperature phase is in $Pnma$ symmetry, in agreement with the early study, but the high-temperature phase adopts $Pcma$ symmetry and twice smaller unit cell.¹¹ Moreover, experimental evidence of complex magnetic ordering below 66 K was also obtained.⁶ Magnetic properties of

RbAgF₃ and CsAgF₃ were only scarcely described in the structure determination paper.¹⁰ The main obstacle while analysing magnetic properties of RbAgF₃ and CsAgF₃ was that that samples were contaminated with M₂AgF₄ and M₃AgF₇ (M = Rb, Cs) phases. The M₂AgF₄ phases are ferromagnetic,⁴ thus obscuring magnetic signals from antiferromagnetic MAgF₃ ones.

A recent theoretical study of MAgF₃ compounds assumed the previously proposed crystal structures and it mostly focused on their magnetic properties. It seems that all compounds from the MAgF₃ family can be regarded as quasi-1D antiferromagnets, with strong AFM intra-chain superexchange, and much weaker FM inter-chain one.⁵ The calculated intra-chain superexchange constant J_{1D} is impressively large, varying between -113 meV for KAgF₃, via -144 meV for RbAgF₃, and reaching -161 meV for CsAgF₃. In all cases the inter-chain superexchange constants do not exceed +10 meV. Compounds exhibiting such strong magnetic interactions are rare and are of interest for solid state physics; when appropriately modified, they could be used in spintronics e.g. for data storage.

The above-mentioned theoretical study⁵ puts in question the tetragonal unit cell of RbAgF₃; authors have noticed that an orthorhombic polymorph of RbAgF₃ has lower total energy than the tetragonal one. One possible reason for this is that experimental study¹⁰ has been conducted at 293 K, while theoretical one corresponds formally to 0 K. Another reason might be the poor quality of old X-ray data, which did not permit to detect small orthorhombic distortion of the tetragonal cell.

In our recent work, we have studied lattice dynamics of KAgF₃ in order to understand its phase transition and to assign vibrational modes.¹⁴ Very good agreement between theory and experiment was reached. Phonon calculations also proved stability of the low temperature orthorhombic polymorph of KAgF₃. As up to now, no lattice dynamics studies of RbAgF₃ and CsAgF₃ were performed, we have decided to conduct a joint experimental/theoretical study of these compounds. The goal of this study is to expand our recent work on KAgF₃ by assigning vibrational spectra of RbAgF₃ and CsAgF₃ and to gain better understanding of RbAgF₃ crystal structure. Moreover, by comparing the data for all three members of the MAgF₃ family, we aimed to detect trends in chemical bonding and vibrational structure across the series.

As a bonus, we have been able to determine crystal structure of Rb₃Ag₂F₇ Ruddlesden-Popper phase, support the space group assignment using theoretical density functional theory (DFT) calculations, and calculate the magnetic superexchange constant for discrete Ag₂F₇³⁻ dimers present in its structure.

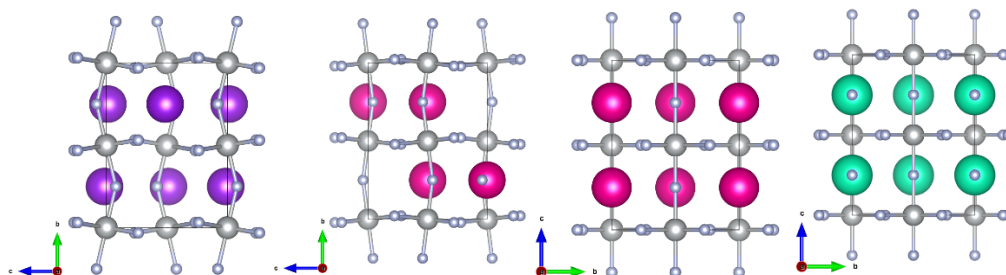


Figure 1. Crystal structures of (from left): KAgF₃ (in low temperature *Pnma* space group), RbAgF₃ (in theoretically predicted *Pnma* space group), RbAgF₃ (in experimental *I4/mcm* space group), and CsAgF₃ (*I4/mcm*). Colour coding: grey – silver, light blue – fluorine, violet – potassium, pink – rubidium, cyan – caesium.

2. Experimental

KAgF₃ syntheses were conducted in three different ways: (1) annealing of ground mixture KF and AgF₂ at 300°C for four days in a nickel reactor under F₂ atmosphere, (2) thermal decomposition of KAgF₄ maintaining dynamic vacuum at 420°C, (3) fluorination of KAg(CN)₂ with stoichiometric quantity of fluorine gas at 300°C. RbAgF₃ sample was synthesized by annealing of hand ground RbF and AgF₂ mixture. This was conducted in a nickel boat in a nickel autoclave for 24 h at 310°C. After that time resultant mixture was ground again and annealed in the same reaction for additional 24 h. CsAgF₃ synthesis was conducted by annealing of hand ground mixture of CsF and AgF₂ (same conditions as RbAgF₃) or thermal decomposition of CsAgF₄ (same conditions as KAgF₃). Better purity CsAgF₃ sample was obtained from the first approach.

Infrared measurements were carried out on Bruker Vertex 80 V vacuum spectrometer using powdered samples placed on cleaned and dried HDPE windows.

Raman spectra for KAgF₃ and RbAgF₃ were obtained on a Horiba Yvon LabRam-HR Raman micro-spectrometer with 632.8 nm He-Ne exciting beam. Due to technical issues with abovementioned spectrometer, spectrum for CsAgF₃ was obtained on Renishaw inVia micro-spectrometer with 785 nm excitation beam. Because of contamination of RbAgF₃ and CsAgF₃ samples with small amounts of Rb₂AgF₄ and Cs₂AgF₄

double perovskites, and triple perovskite $\text{Rb}_3\text{Ag}_2\text{F}_7$ Raman spectra varied somewhat from one measurement spot to another. Results chosen for further analysis were crosschecked with published data to confirm that we indeed measured spectra for MAgF_3 rather than M_2AgF_4 crystallites.¹⁴⁻¹⁶

Low temperature Raman spectra were measured in a custom setup described in our recent work¹⁴ using Horiba Yvon LabRam-HR Raman micro-spectrometer with 632.8 nm He-Ne exciting beam. Setup consists of FEP tube equipped with capillary holder, dry air cooled by LN_2 and a thermocouple.

Room temperature powder X-ray diffraction measurements were carried out on Bruker D8 Discover diffractometer, using $\text{CuK}\alpha$ radiation. Sample was placed in heat sealed in prefluorinated 0.3 mm quartz capillary. Measurement 2σ range spanned from 6° to 90° , with step size of 0.014° . Acquisition time used here was equal to 16 h for whole measurement in four consecutive runs to determine if sample reacted with the capillary. Low temperature measurements were conducted on Oxford Diffraction Xcalibur 2 single crystal diffractometer also using $\text{CuK}\alpha$ radiation. Resolution of these measurements is worse than room temperature measurements, because detectors in these diffractometers are usually placed much closer to the sample. Using this setup had an advantage of reaching 80 K with high accuracy.

Room temperature powder data was refined using Rietveld method¹⁷ in Fullprof software suite.¹⁸ Full set of profile (including asymmetry) and atomic (positions and isotropic thermal factors) parameters were refined. Absorption correction factor of $\mu\text{R} = 1.1$ was used.

3. Computational details

Lattice dynamics of MAgF_3 ($\text{M} = \text{K}, \text{Rb}, \text{Cs}$) compounds was modelled using hybrid functional HSE06,¹⁹ based on Perdew-Burke-Ernzerhof DFT-GGA functional revised for solids (PBEsol)²⁰ with 25% Hartree Fock exchange energy. For all calculations, projector-augmented-wave method^{21,22} was used, as implemented in VASP 5.4.4 code.²³⁻²⁵ Standard VASP pseudopotentials were used for description of core electrons.

All structures were optimized by performing a full relaxation of unit cell parameters and atomic coordinates. Antiferromagnetic (AFM) ordering was assumed for all structures in agreement with previous results (i.e. AFM ordering within chains propagating along the crystallographic c direction, and ferromagnetic (FM) one within sheets parallel to ab planes).^{5,26} The cut-off energy of the plane wave basis set was equal to 520 eV with a self-consistent-field convergence criterion of $1 \cdot 10^{-7}$ eV. The k-point mesh spacing used in calculations was equal to 0.25 \AA^{-1} . All structures were optimized until the forces acting upon each atom were smaller than 0.001 eV/\AA .

Phonon calculations were conducted using finite differences method implemented in VASP. Results were then processed using Phonopy package in order to extract irreducible representations and dispersion curves, as VASP provides frequencies only in the centre of the first Brillouin zone (Γ point).²⁷ Animated pictures of normal modes, also generated by Phonopy, were used to assign mode types. Calculations were conducted for single unit cells, in order to limit resource usage. Phonon band structures were calculated for standardized k-path.²⁸ For tetragonal I -centered cells, primitive cells ($Z=2$) were used for band structure and irreducible representations calculations.

Magnetic superexchange constants were calculated using broken symmetry method mapping calculated energy values on spin Hamiltonian in a form:

$$H = -0.5 \sum_{i,j} J_{ij} s_i s_j$$

Total energy values for each magnetic configuration were obtained by the means of GGA+U by conducting single point calculations using geometry of ground state configuration. The k-point mesh spacing used in calculations was equal to 0.16 \AA^{-1} . The cut-off energy of the plane wave basis set was equal to 800 eV with a self-consistent-field convergence criterion of $1 \cdot 10^{-7}$ eV.

4. Results and discussion

4.1. Theoretical phonon spectra.

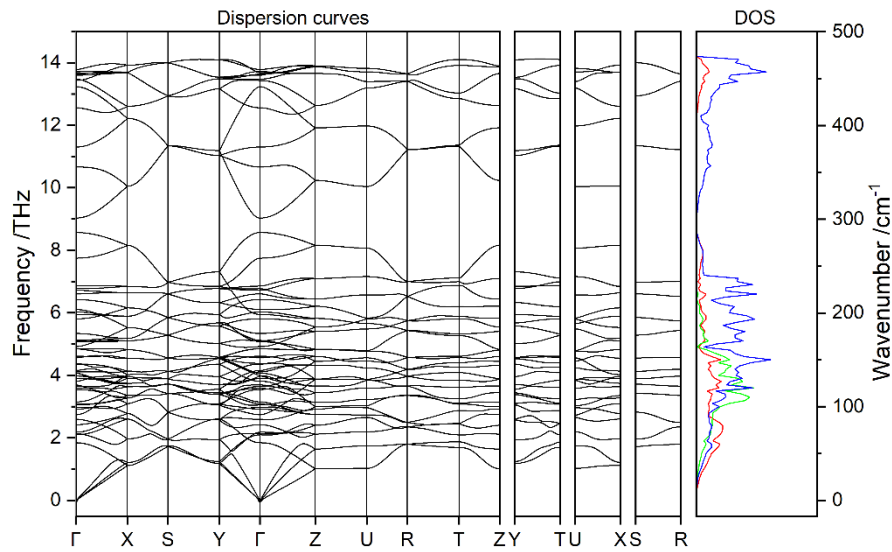


Figure 2. Calculated phonon dispersion curves and (atomic) phonon density of states for KAgF_3 (blue – F, red – Ag, green – K)

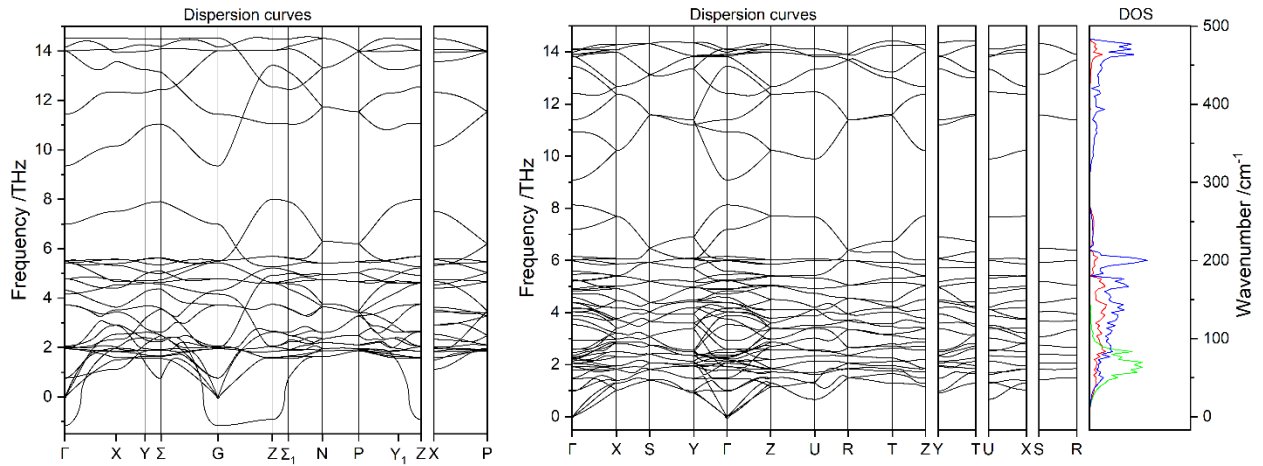


Figure 3. Calculated phonon dispersion curves for tetragonal RbAgF_3 (left), and combined graph of dispersion curves and phonon density of states for orthorhombic RbAgF_3 (right) (blue – F, red – Ag, green – Rb)

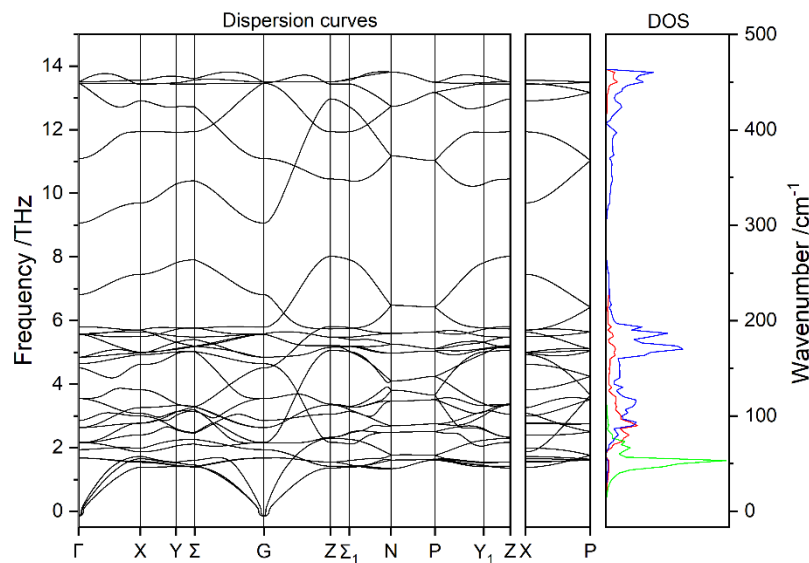


Figure 4. Calculated phonon dispersion curves and (atomic) phonon density of states for tetragonal CsAgF_3 (blue – F, red – Ag, green – Cs)

Dispersion curves calculated for KAgF_3 using HSE06 dataset and Phonopy suite (Figure 2), remain in a good agreement with those computed recently utilizing a commercial PHONON software.¹⁴ All features of phonon density of states were also successfully reproduced. Therefore, for the remaining systems their phonon spectra were computed using Phonopy.

Our lattice dynamics calculations using published, tetragonal structure of RbAgF_3 show significant dynamic instability at the centre of the first Brillouin zone (Γ) but also in other special points (Figure 3, top). The presence of an imaginary branch alone is the proof that the tetragonal structure cannot be the ground state of this system. Due to that, we have used a modified model in which we have allowed for the presence of kinked $[\text{AgF}_3^-]$ chains similar to those typical of KAgF_3 . Full geometry relaxation using HSE06 functional yielded a dynamically stable structure (Figure 3, bottom), that had 11.7 meV per unit cell ($Z=4$) lower total energy than the starting tetragonal one. That energy difference corresponds roughly to a temperature of 34 K, so it may be deduced that the orthorhombic form corresponds to a low temperature polymorph. As a result of larger ionic radius, the $[\text{AgF}_3^-]$ chains in theoretically calculated RbAgF_3 are less kinked than in calculated KAgF_3 (165.5° vs. 153.3°). This effect can also be seen by analysing density of states graph. Vibrational states of Rb are more localized than those of K signalling a larger freedom of potassium ions in KAgF_3 for rattling.

Phonon dispersion curves calculated for a primitive cell of tetragonal CsAgF_3 (Figure 4) confirm dynamic stability of this structure. A small departure of one mode from null value ($\text{img } 5 \text{ cm}^{-1}$) stems from imperfect diagonalization of Hessian matrix, and may be considered artefactual. Localization of alkali metal vibrational states is in CsAgF_3 even more apparent meaning that caesium, with its large ionic radius, sits tightly in interstitial positions. Consequently, Ag-F-Ag angles present here are straight (*i.e.* 180°). This comes from the fact that among alkali metal cations, the Cs(I) cation best fulfils the geometric condition of structural stability of a perovskite structure.

Due to similarity in MAgF_3 ($M = \text{K, Rb, Cs}$) structures, normal modes involving similar atomic displacements can be found in each spectrum (Figure 5). In the highest wavenumber region ($425\text{--}475 \text{ cm}^{-1}$) modes calculated for RbAgF_3 corresponding to stretching vibrations of the Ag-F bond network exhibit higher energies than those for KAgF_3 and CsAgF_3 . This is an interesting feature which may be explained by considering that there are two main factors in play in the $M = \text{K, Rb, Cs}$ series. One factor is related to the Lewis acidity of $M(\text{I})$ cations. K(I) cation having the largest Lewis acidity in the series leads to its strongest interaction with F^- ions and thus to some weakening of the Ag-F bonds. Volume of the $M(\text{I})$ cation is the other factor, \ddagger ²⁹ which – particularly for the largest Cs(I) cation, may also induce weakening of the Ag-F bonds due to “negative pressure” exerted by this cation. It seems that the problem of two mutually opposing factors has an optimum and the Rb(I) salt shows the highest frequencies of Ag-F stretching modes.

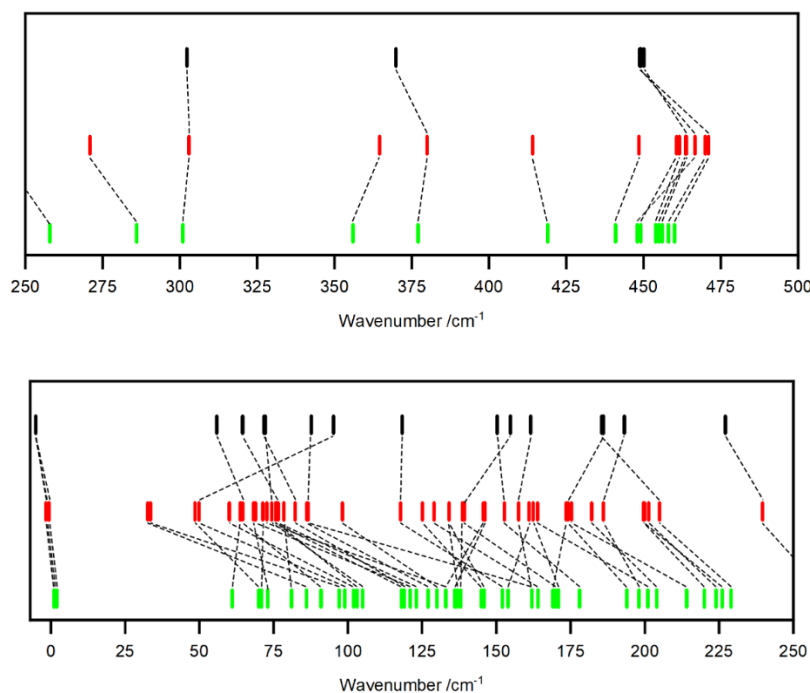


Figure 5. Calculated wavenumber of normal modes at Γ for orthorhombic KAgF_3 (green), orthorhombic RbAgF_3 (red) and tetragonal CsAgF_3 (black). Dashed lines connect corresponding modes with similar forms of vibrations. Note that the number of modes computed for CsAgF_3 in its primitive cell is twice smaller than those for orthorhombic K and Rb ones, hence some modes do not have counterparts in the spectrum of Cs derivative.

Midrange $[\text{AgF}_6]$ octahedron stretching modes ($300\text{-}425\text{ cm}^{-1}$) are generally close in energy for all three compounds. However, finding the modes corresponding to one another in the spectral region below 250 cm^{-1} (e.g. lattice modes) is not that straightforward, because of significant admixture of heavy alkali metal vibrations in each mode. Generally normal modes found for RbAgF_3 are softer than analogous modes of KAgF_3 in agreement with the *ca.* twice reduced oscillator mass for the latter. Corresponding modes of CsAgF_3 have comparable values to those for Rb analogue.

4.2. Assignment of vibrational spectra.

Our analysis of powder x-ray pattern shows that at room temperature RbAgF_3 adopts tetragonal structure. As stated above, this is supposedly a high-temperature form, with orthorhombic one corresponding to the genuine ground state at $T \rightarrow 0\text{ K}$. Since our spectroscopic measurements were conducted at room temperature, we have used phonons calculated for tetragonal polymorph for an interpretation of IR and Raman data.

Infrared spectrum measured for RbAgF_3 consists of 8 bands, while Raman measurement yielded 6 bands (Figure 7). Group theory analysis for that compound in a primitive cell of the $I4/mcm$ space group yields 21 distinct normal vibrational modes, including some degenerated ones ($\Gamma_{\text{acoustic}} = A_{2u} + E_u$; $\Gamma_{\text{optic}} = A_{1g} + 2A_{2g} + 3A_{2u} + B_{1g} + 2B_{1u} + 2B_{2g} + 5E_u + 3E_g$); here, there are 7 Raman active ($A_{1g}, B_{1g}, 2B_{2g}, 3E_g$) and 8 IR-active modes ($3A_{2u}, 5E_u$). The remaining modes are silent. Measured spectra for CsAgF_3 in $I4/mcm$ symmetry consist of 9 infrared bands and 4 Raman bands. Obviously, the group theory predicts identical result as for the Rb salt.

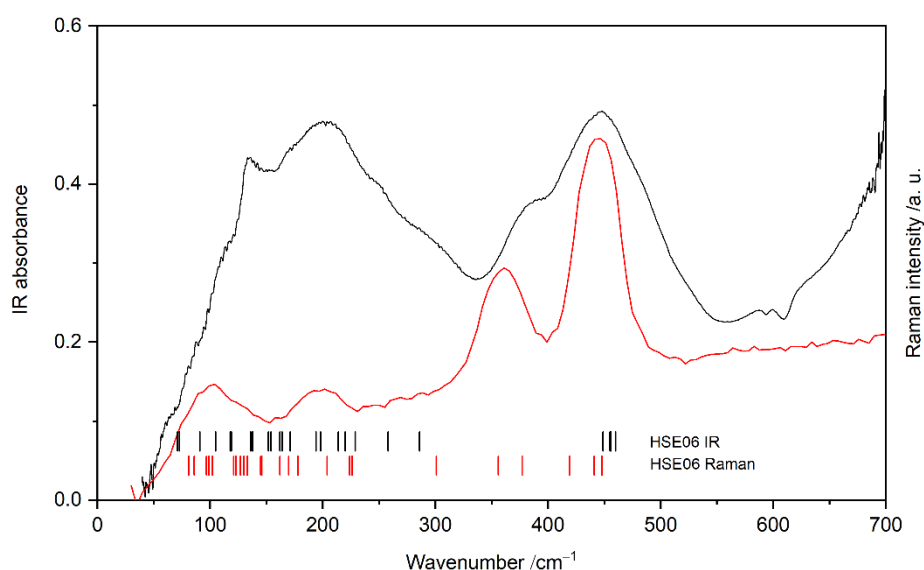


Figure 6. FIR (black) and Raman (red) spectra of KAgF_3 at room temperature together with marks indicating the computed wavenumbers.

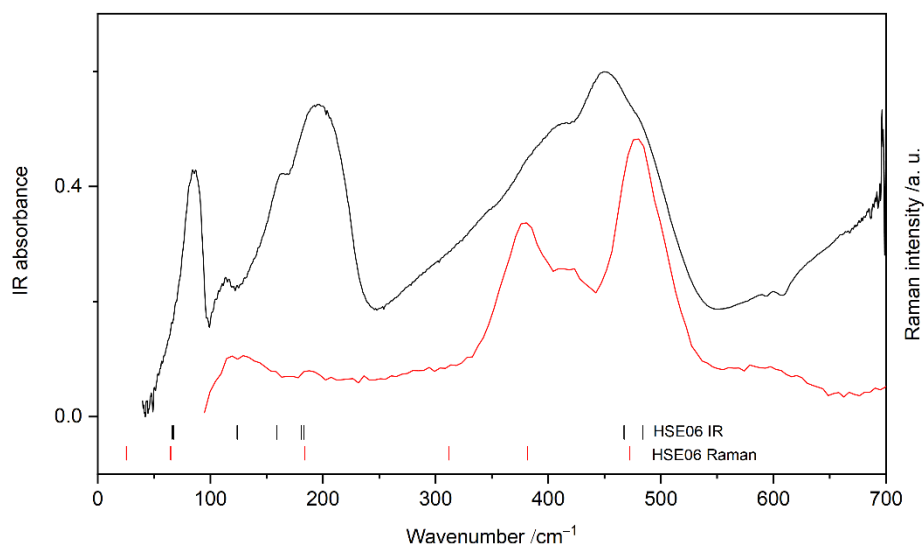


Figure 7. FIR (black) and Raman (red) spectra of RbAgF_3 at room temperature together with marks indicating the computed wavenumbers.

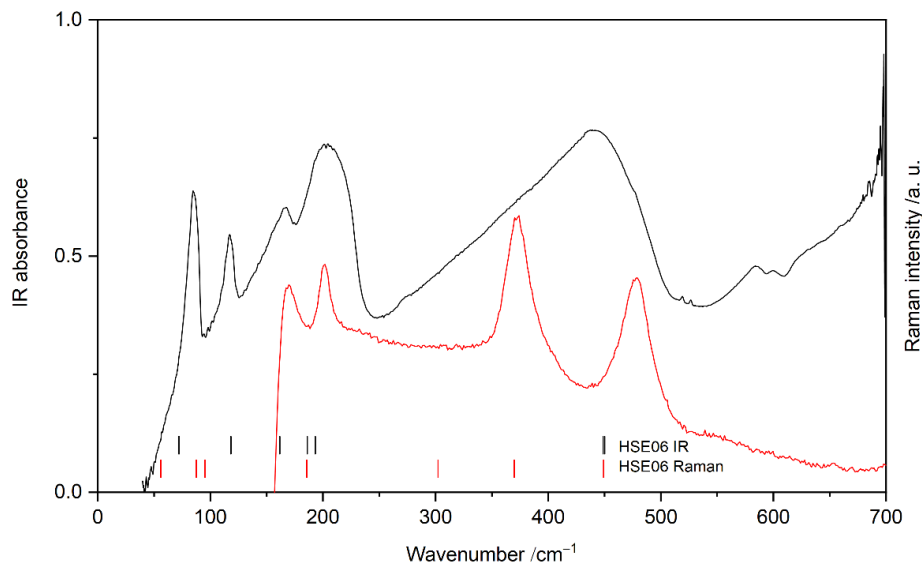


Figure 8. FIR (black) and Raman (red) spectra of CsAgF₃ at room temperature together with marks indicating the computed wavenumbers. The Raman spectrum for Cs salt shows an abrupt decline in intensity below 170 cm⁻¹ due to a notch filter.

KAgF₃ spectra were described in detail in our recent work based on DFT+U and HSE06 calculations.¹⁴ Here, in Figure 6, we show the experimental spectra overlapped with theoretically predicted modes using highly accurate hybrid HSE06 functional (without any scaling factor), so that they may be compared with those measured for its heavier analogues.

Out of eight infrared bands present in RbAgF₃ spectrum (Figure 7), six were successfully assigned to fundamentals and two to combination modes (using group theory constraints for selection rules) or impurities (Table 1). The highest wavenumber band in infrared spectrum is placed at 460 cm⁻¹ and was assigned to E_u mode representing Ag–F stretching within [AgF₂] planes. Three midrange bands at 200, 162 and 113 cm⁻¹ correspond to bending modes assigned to A_{2u} [AgF₂] plane buckling, E_u [AgF₂] in plane bending and E_u [AgF₆] octahedron bending respectively. The lowest wavenumber bands (85 and 72 cm⁻¹) are rubidium lattice modes. The Raman spectrum features nine six of which three were assigned to fundamentals. The band at 477 cm⁻¹ has the largest intensity; it is assigned to [AgF₆] octahedron stretching mode. The second highest intensity band located at 378 cm⁻¹ was assigned to [AgF₂] plane stretching. In the lower wavenumber range, there is one band at 189 cm⁻¹ which was assigned to [AgF₆] octahedron bending mode.

Infrared spectrum of CsAgF₃ (Figure 8) consists of nine bands, six of which were successfully assigned to corresponding fundamental modes and three either to combination/overtone modes or impurities (Table 2). The highest wavenumber infrared fundamental at 448 cm⁻¹ falls very close to two predicted normal modes, leaving some ambiguity in assignment; it can either be a [AgF₂] plane stretching or [AgF⁺] chain stretching mode. Similarity to the Rb and K salt suggest preference for the former assignment. Band seen at 206 cm⁻¹ is [AgF₂] plane buckling mode, 163 cm⁻¹ is [AgF₆] octahedron bending mode, and 117 cm⁻¹ is [AgF⁺] chain bending mode. Two lowest energy bands at 86 and 80 cm⁻¹ are Cs lattice modes. Raman spectrum was deconvoluted to four major bands, of which three were assigned to fundamentals. Stretching modes are at 477 cm⁻¹ ([AgF₆] octahedron stretching) and 372 cm⁻¹ ([AgF₂] plane stretching). The third band at 202 cm⁻¹ originates from [AgF₆] octahedron bending.

The correlation between theoretically predicted and measured wavenumbers for both the Rb and Cs salt is excellent, testifying that scaling factor is nearly unity (slope factor is 0.975 for Cs, 0.995 for Rb) when using the HSE06 hybrid functional (Figure 9).¹⁴

Table 1. Vibrational band assignment for tetragonal RbAgF₃ (at room temperature).

IR /cm ⁻¹	Raman /cm ⁻¹	Type	HSE06 /cm ⁻¹	Symmetry	Assignment
	602	w	-	-	impurity
	507	sh	-	-	impurity (possible Rb ₃ Ag ₂ F ₇)
	477	s	472	B _{2g}	[AgF ₆] octahedron stretching
460		s	467	E _u	[AgF ₂] plane stretching
	423	w	-	-	impurity
395		sh	-	-	combination 200+189 (A _{2u} x E _g) or impurity

	378	s	381	A _{1g}	[AgF ₂] plane stretching
347		sh	-	-	combination 162+189 (E _u x E _g) or impurity
200		s	183	A _{2u}	[AgF ₂] plane buckling
	189	m	184	E _g	[AgF ₆] octahedron bending
162		sh	159	E _u	[AgF ₂] in plane bending
113		w	124	E _u	[AgF ₆] octahedron bending
85		s	67	A _{2u}	Lattice (Rb out of plane)
72		sh	66	E _u	Lattice (Rb in plane)

Table 2. Vibrational band assignment for tetragonal CsAgF₃ (at room temperature).

IR /cm ⁻¹	Raman /cm ⁻¹	Type	HSE06 /cm ⁻¹	Symmetry	Assignment
580		w	-		combination 206+372 (A _{2u} x A _{1g}) or impurity
	477	s	449	B _{2g}	[AgF ₆] octahedron stretching
448		s	450	E _u	[AgF ₂] plane stretching
			449	A _{2u}	[AgF ⁺] chain stretching
	398	sh	-	-	overtone (206 A _{2u} x A _{2u}), overtone 202 (E _g x E _g) or impurity
381		sh	-	-	impurity
	372	s	370	A _{1g}	[AgF ₂] plane stretching
318		sh	-	-	combination 117+202 (E _u x E _g) or impurity
206		s	193	A _{2u}	[AgF ₂] plane buckling
	202	m	186	E _g	[AgF ₆] octahedron bending
163		m	162	E _u	[AgF ₆] octahedron bending
117		m	118	E _u	[AgF ⁺] chain bending
86		s	72	A _{2u}	Lattice (Cs out of plane)
80		sh	72	E _u	Lattice (Cs in plane)

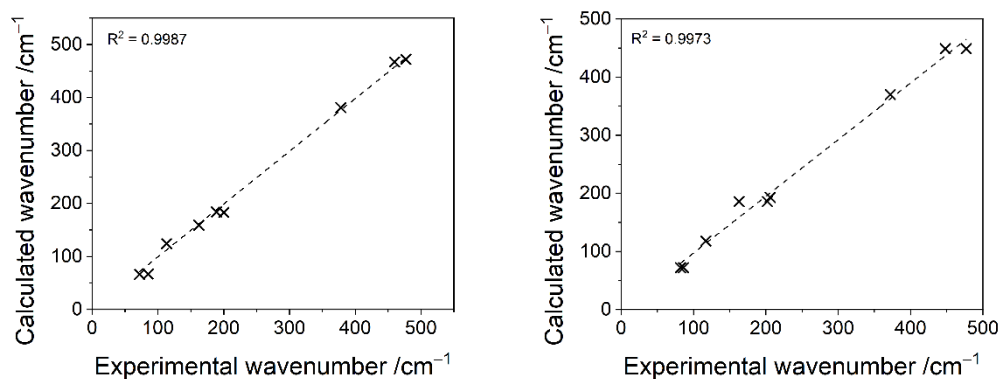


Figure 9. Correlations between theoretical and experimental wavenumbers jointly for IR and Raman spectra (left – RbAgF₃; right – CsAgF₃; black dotted line—linear regression R² depicted at the figure both bound to pass at (0,0)).

4.3. Vibrational spectra and x-ray diffraction pattern for RbAgF₃ at low temperature.

The calculated total energy at 0 K of tetragonal RbAgF₃ is higher than total energy of orthorhombic polymorph. In order to get further insight into a possible tetragonal/orthorhombic phase transition, low temperature Raman spectrum (at 154 K) and low temperature x-ray diffraction pattern (at 80 K) were measured.

Comparison of low temperature Raman spectrum with that measured at room temperature shows the expected stiffening of all modes (Figure 10). Two features of highest energy got shifted towards higher wavenumber range (from 378 to 382 cm⁻¹ and from 477 to 488 cm⁻¹; a similar stiffening was observed before for the K salt.¹⁴ Spectral features are better resolved in low-T spectra, as expected. Most new bands appear in the region above 600 cm⁻¹, where no fundamentals can be found; they correspond to either combination modes or overtones (*cf.* ESI). These changes are not dramatic, and take place gradually while cooling down the sample

(all spectra measured are available in ESI). While these measurements did not prove that a phase transition might occur, they also did not disprove such possibility, since the Raman spectra of orthorhombic KAgF_3 and of tetragonal RbAgF_3 do not differ markedly. Because of that, we have also conducted low temperature powder X-ray diffraction experiment at 80 K.

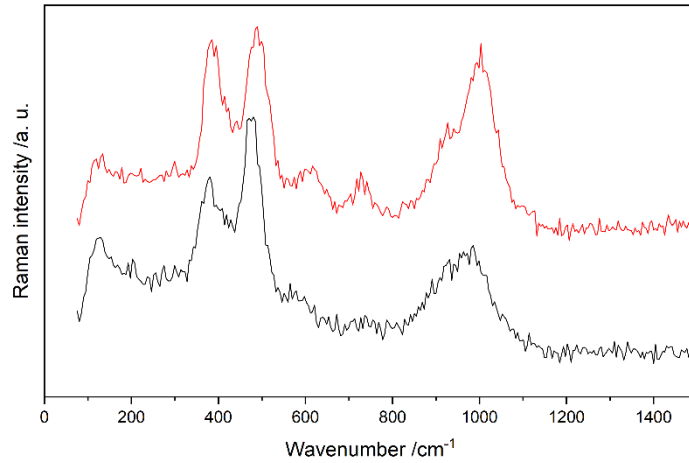


Figure 10. Raman spectrum of RbAgF_3 measured at room temperature (black) and at 154 K (red).

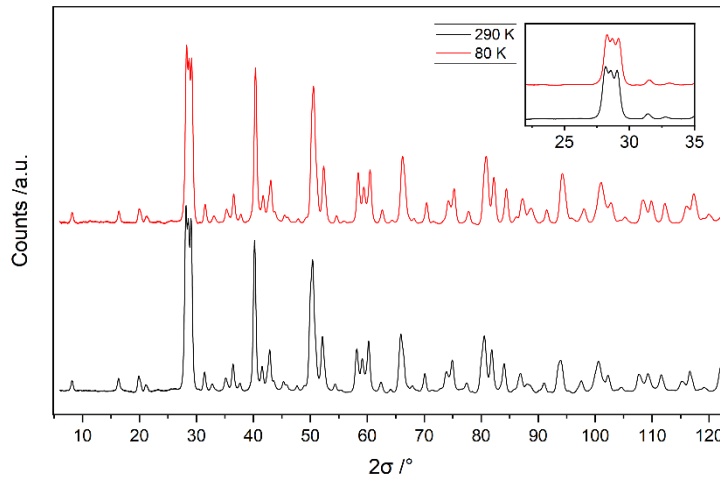


Figure 11. Background-reduced powder x-ray diffraction pattern of RbAgF_3 measured at room temperature (black) and at 80 K (red). Inset shows the three most intense peaks of the pattern.

We were able to reach temperature of 80 K in powder X-ray diffraction measurements (Figure 11). Resolution of that pattern is sufficient for the analysis of a possible tetragonal-to-orthorhombic transition. Theory predicts that a splitting of a tetragonal lattice parameter to two distinct values of 6.263 Å and 6.344 Å (\mathbf{a} and \mathbf{c} vectors in the $Pnma$ setting) will affect most strongly the 100 vs. 001, 110 vs. 011, 002 vs. 200, and related pairs of reflections. Unfortunately, they all fall in 2 theta regions where the reflections from the impurity phase are also present (see the next section). Therefore, X-ray analysis is also inconclusive with respect to a possible symmetry-lowering transition. Much purer specimen of RbAgF_3 and likely much lower temperature, is needed for such detection. The only unambiguous phenomenon observed is that of the thermal expansion; for example, tetragonal lattice constant of RbAgF_3

expands by 0.18 % upon warming while the perpendicular lattice vector by 0.33 %; such anisotropy is, obviously, not unexpected, given that \mathbf{b} is axis of propagation of the AgF_3^- infinite chains which \mathbf{a} and \mathbf{c} are equivalent.

4.4. Crystal structure and magnetic properties of the Ruddsden-Popper phase $\text{Rb}_3\text{Ag}_2\text{F}_7$.

One of the studied samples of RbAgF_3 showed significant proportion of an impurity phase. This additional phase was not only seen in PXRD measurements, but also during Raman experiments. Since Raman spectrometers equipped with microscope collect data from only a small micron-sized surface spot, it is sometimes possible to identify different phases present in the samples. We have managed, for example, to observe a distinct feature located at 504–507 cm^{-1} (*cf.* ESI). This feature was above the range of the theoretically predicted stiffest Raman-active phonon (477 cm^{-1}), but its wavenumber might correspond to the

Ag–F stretching of slightly shorter Ag–F bonds than those present in RbAgF_3 . This fact, together with the substantial number of unassigned reflections in the X-ray diffraction pattern, led us to more detailed study of the new phase. Indexation of the unassigned reflections yielded a strongly elongated tetragonal unit cell. Structural database search pointed out at a similar phase of the $\text{K}_3\text{Ag}_2\text{F}_7$ stoichiometry, which some of us first detected two decades ago. This phase was subsequently refined in the $Ccca$ space group.⁷ Additional research conducted over the next decade shown that the $Ccca$ cell is certainly erroneous since it contains Ag(II) sites in an compressed rather than usual elongated octahedral environment.

A very similar conclusion was reached with respect to K_2AgF_4 double perovskite.^{7,8,13} Equipped with this knowledge, and aided by DFT+U calculations, we have been able to provide a $Cmca$ starting model for the novel $\text{Rb}_3\text{Ag}_2\text{F}_7$ phase. This model was then used in Rietveld refinement of that pattern (full fit and crystallographic information file are available in ESI) and resulted in the structure which closely matched a theoretical one (*cf.* ESI for all theoretically derived .cif files).

Orthorhombic $\text{Rb}_3\text{Ag}_2\text{F}_7$ is a typical Ruddlesden-Popper phase (Figure 12), *i.e.* an intergrowth of the RbAgF_3 and Rb_2AgF_4 end members of the series. Its formation, while trying to prepare RbAgF_3 , may be explained by partial reduction of Ag(II)F_2 to Ag(I)F upon reaction with walls of the reactor. In consequence, some RbF is left unreacted but its amount does not suffice for the formation of Rb_2AgF_4 . Instead, a 50:50 compound is formed. This structure can be described as infinite $[\text{AgF}_2]$ double (sandwich) layers interleaved with rubidium fluoride layers. Each pair of layers is rotated by 45° in respect to the neighbouring ones. The $[\text{AgF}_6]$ octahedra are distorted in a way already known from RbAgF_3 and Rb_2AgF_4 . Apical fluorides have varying atomic distances to Ag(II) of 2.19(3) and 2.104(4) Å (the shortest distance is that in between sandwich layers). There are two different equatorial Ag–F distances of 2.20(3) and 2.35(3) Å. Apical fluorides form a straight link between Ag sites, but the layers are buckled with the intrasheet Ag–F–Ag angle of $163.4(14)^\circ$ angle (theoretical value 177°).

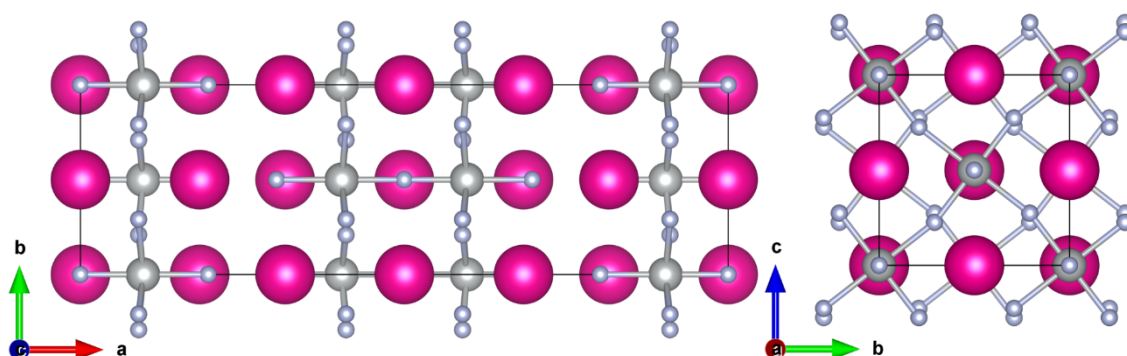


Figure 12. Crystallographic unit cell of novel $\text{Rb}_3\text{Ag}_2\text{F}_7$ phase (pink – rubidium, grey – silver, blue – fluorine).

Table 3. Crystallographic data for novel $\text{Rb}_3\text{Ag}_2\text{F}_7$.

Formula	$\text{Rb}_3\text{Ag}_2\text{F}_7$
Colour	brown
Space group	$Cmca$ (No. 64)
Z	4
$V / \text{\AA}^3$	879.524(18)
$a / \text{\AA}$	21.7577(5)
$b / \text{\AA}$	6.35844(9)
$c / \text{\AA}$	6.35747(9)
$\alpha / ^\circ$	90
$\beta / ^\circ$	90
$\gamma / ^\circ$	90
Positions	Rb1 0.68404(15) 0.00000 0.00000 Rb2 0.50000 0.00000 0.00000 0.00776 Ag1 -0.09670(16) 0.00000 0.00000 F1 0.8028(13) 0.00000 0.00000 F2 0.00000 0.00000 0.00000 F3 0.5899(7) 0.291(4) 0.274(5)

Reliability factors	Not corrected for background (all data) R _P = 0.84 % R _{wp} = 1.78 %
	Corrected for background (all data) cR _P = 27.86 % cR _{wp} = 15.16 % R Bragg factor (this phase) R _{Bragg} = 15.81 %
Atomic distances /Å	Ag–F (apical) 2.19(3) 2.104(4)
	Ag–F (equatorial) 2.20(3) 2.35(3)

The shortest Ag–F distance of 2.104(4) Å is slightly shorter than the shortest distance of 2.10935(3) Å seen in tetragonal RbAgF₃ at a room temperature. This, together with the different reduced mass factor, might explain why the corresponding oscillator for Rb₃Ag₂F₇ is stiffer by 5% than that seen for RbAgF₃, as explained above.

Consideration of Goodenough–Kanamori–Anderson rules leads us to the notion, that magnetic interaction between two [AgF₂] layers within a sandwich must be very strong and antiferromagnetic. Indeed, the computed magnetic ground state of Rb₃Ag₂F₇ turns out to feature an antiferromagnetic spin ordering in [Ag₂F₇] dimers, ferromagnetic within [AgF₂] layers, and also weakly ferromagnetic between sandwich layers (*i.e.* in a (AB)(BA) manner). Because of that, we have simplified calculations by assuming two dominant superexchange pathways: Ag–F–Ag within a dimer along crystallographic *a* axis (this coupling constant is labelled J_{0D}), and an intralayer Ag–F...Ag one (labelled J_{perp}). Superexchange constants are expressed by equations:

$$J_{0D} = \frac{E_{A2} - E_{A1}}{8}, \quad J_{perp} = \frac{E_{A1} - E_{FM}}{2}$$

(E_{A1} is total energy of the ground state, E_{A2} is total energy ordered antiferromagnetically in dimers, antiferromagnetically in layers, E_{FM} is total energy of ferromagnetic solution; energy values per unit cell).

Calculated values are J_{0D} = –240.2 meV, J_{perp} = 10.9 meV. The J_{0D} value is comparable with those for other strongly coupled Ag(II)-based antiferromagnets calculated to date. Related fluoroargentate(II) systems showing low magnetic dimensionality are Ag₂ZnZr₂F₁₄ (J_{0D} = –313 meV), HPtII-AgF₂ (J_{0D} = –250 meV) phase,³⁰ AgFBF₄ (J_{1D} = –298 meV)⁵ and CsAgF₃ (J_{1D} = –161 meV).⁵ On the other hand, J_{perp} is ferromagnetic and comparable to a several meV values typical for MAgF₃⁶ and M₂AgF₄.⁸ The ratio of J_{perp} and J_{0D} is *ca.* 0.045 and permits us to label this system as quasi-0D because dimers interact with each other quite weakly.

5. Conclusions

Theoretical calculations have led us to conclusion, that at the T → 0 K limit, the previously published structure of RbAgF₃¹⁰ is not dynamically stable (in a harmonic approximation). We have been able to propose orthorhombic candidate for the low temperature polymorph, that is isostructural to low-temperature form of KAgF₃. Main structural difference between both forms reveals itself in Ag–F–Ag chains, which in tetragonal RbAgF₃ are completely straight, and kinked in orthorhombic RbAgF₃. There is also an associated puckering of the [AgF₂] sheets in the orthorhombic polytype. Total energy of that orthorhombic phase is 11.7 meV lower than that of the known tetragonal counterpart (HSE06, per Z=4 unit cell), which corresponds to 0.3 kJ mol^{–1} or 34 K.

In order to experimentally confirm a possible existence of low temperature RbAgF₃ polymorph, low temperature Raman and powder X-ray diffraction study were conducted. Unfortunately, both methods were inconclusive. Colling to liquid helium temperatures and preparing of a purer specimen is needed to confirm or refute the postulated phase transition. Orthorhombic RbAgF₃ should be searched for at LHe temperatures.

Comparative theoretical analysis of lattice dynamics of MAgF₃ (M = K, Rb, Cs) compounds was performed. Phonon dispersion curves, phonon density of states and full list of vibrational modes were calculated for orthorhombic RbAgF₃ and tetragonal CsAgF₃ as a development of our recent study for the K analogue.¹⁴

Analysis of phonon density of states graph yielded conclusion, that having larger cation in interstitial positions in a distorted perovskite lattice causes significant localization of certain phonons. We have also compared corresponding theoretically predicted modes to understand trends observed in that series of compounds.

Although at 0 K the orthorhombic RbAgF₃ is more stable, in order to analyse room temperature spectral data it was necessary to calculate normal modes for tetragonal structure. Using that, and predicted phonons for CsAgF₃ we have assigned specific vibrations to most bands present at IR and Raman spectra. We have reached very good accuracy of the correlation between experimental and theoretical data, thus supporting our assignment.

One of analysed samples of RbAgF₃ contained significant portion of contamination phase. Upon indexation, DFT+U modelling, and subsequent Rietveld refinement we have proposed a novel Rb₃Ag₂F₇ phase. This new compound constitutes the second known Ruddlesden-Popper phase in fluoroargentate(II) family. Rb₃Ag₂F₇ crystallizes in *Cmca* (No. 64) space group (21.7577(5) 6.35844(9) 6.35747(9) 90 90 90). Its structure best described as sandwich layers of [AgF₂] stacked at 45°, interleaved with rubidium cations. According to the DFT calculations, this compound features one of the shortest Ag–F bonds known, and it hosts a very strong antiferromagnetic superexchange ($J_{\text{OD}} = -240.2$ meV) within the sandwich layers.

6. Acknowledgements

Powder X-ray diffraction measurements were carried out on The Jan Czocharski Laboratory For Advance Crystal Engineering equipment.

Polish authors are grateful to NCN for support (Maestro, 2017/26/A/ST5/00570). Slovenian authors acknowledge the Slovenian Research Agency for financial support within research program P1-0045 Inorganic Chemistry and Technology. Calculations were performed using ICM UW supercomputing resources (oceanos, projects GA76-19 and GA83-34).

7. Notes and references

Further details of the crystal structures reported here may be obtained from Fachinformationszentrum Karlsruhe (76344 Eggenstein-Leopoldshafen, Germany; fax (+49)7247-808-666; e-mail: crysdata@fizkarlsruhe.de) on quoting their CSD numbers: 2122449 for RbAgF₃ and 2122450 for Rb₃Ag₂F₇.

‡ Ionic radius of MAgF₃ (M = K, Rb, Cs) compounds increases in the series starting from 1.64 Å for potassium, through 1.72 Å for rubidium, to 1.88 Å for caesium (all for coordination number XII).

- 1 J. Gawraczyński, D. Kurzydłowski, W. Gadomski, Z. Mazej, G. Ruani, I. Bergenti, T. Jaroń, A. Ozarowski, S. Hill, P. J. Leszczyński, K. Tokár, M. Derzsi, P. Barone, K. Wohlfeld, J. Lorenzana and W. Grochala, *Proc. Natl. Acad. Sci.*, 2019, **116**, 1495–1500.
- 2 W. Grochala, R. G. Egdell, P. P. Edwards, Z. Mazej and B. Žemva, *ChemPhysChem*, 2003, **4**, 997–1001.
- 3 N. Bachar, K. Koterka, J. Gawraczyński, W. Trzcinski, J. Paszula, R. Piombo, P. Barone, Z. Mazej, G. Ghiringhelli, A. Nag, K.-J. Zhou, J. Lorenzana, D. van der Marel and W. Grochala, .
- 4 S. E. McLain, M. R. Dolgos, D. A. Tennant, J. F. C. Turner, T. Barnes, T. Proffen, B. C. Sales and R. I. Bewley, *Nat. Mater.*, 2006, **5**, 561–565.
- 5 D. Kurzydłowski and W. Grochala, *Angew. Chemie - Int. Ed.*, 2017, **56**, 10114–10117.
- 6 D. Kurzydłowski and W. Grochala, *Phys. Rev. B*, 2017, **96**, 155140.
- 7 Z. Mazej, E. Goresnik, Z. Jagličić, B. Gaweł, W. Łasocha, D. Grzybowska, T. Jaroń, D. Kurzydłowski, P. Malinowski, W. Koźminski, J. Szydłowska, P. Leszczyński and W. Grochala, *CrystEngComm*, 2009, **11**, 1702–1710.
- 8 D. Kurzydłowski, M. Derzsi, Z. Mazej and W. Grochala, *Dalt. Trans.*, 2016, **45**, 16255–16261.
- 9 D. Kurzydłowski, Z. Mazej and W. Grochala, *Dalt. Trans.*, 2013, **42**, 2167–2173.
- 10 R. H. Odenthal and R. Hoppe, *Monatshefte für Chemie*, 1971, **102**, 1340–1350.
- 11 D. Kurzydłowski, Z. Mazej, Z. Jagličić, Y. Filinchuk and W. Grochala, *Chem. Commun.*, 2013, **49**, 6262–6264.
- 12 A. I. Popov and Y. M. Kiselev, *Zhurnal Neorg. Khimii*, 1987, **32**, 2276.

- 13 W. Grochala, 2001.
- 14 K. Koterias, J. Gawraczyński, M. Derzsi, Z. Mazej and W. Grochala, *Chemistry (Easton)*., 2021, **3**, 94–103.
- 15 D. Kurzydłowski, T. Jaroń, A. Ozarowski, S. Hill, Z. Jagličić, Y. Filinchuk, Z. Mazej and W. Grochala, *Inorg. Chem.*, 2016, **55**, 11479–11489.
- 16 J. Gawraczyński, PhD Thesis, University of Warsaw, 2019.
- 17 H. M. Rietveld, *J. Appl. Crystallogr.*, 1969, **2**, 65–71.
- 18 J. Rodríguez-Carvajal, .
- 19 A. V. Krukau, O. A. Vydrov, A. F. Izmaylov and G. E. Scuseria, *J. Chem. Phys.*, 2006, **125**, 224106.
- 20 G. I. Csonka, J. P. Perdew, A. Ruzsinszky, P. H. T. Philipsen, S. Lebègue, J. Paier, O. A. Vydrov and J. G. Ángyán, *Phys. Rev. B - Condens. Matter Mater. Phys.*, 2009, **79**, 155107.
- 21 P. E. Blöchl, *Phys. Rev. B*, 1994, **50**, 17953–17979.
- 22 G. Kresse and D. Joubert, *Phys. Rev. B - Condens. Matter Mater. Phys.*, 1999, **59**, 1758–1775.
- 23 G. Kresse and J. Hafner, *Phys. Rev. B*, 1993, **47**, 558–561.
- 24 G. Kresse and J. Furthmüller, *Phys. Rev. B - Condens. Matter Mater. Phys.*, 1996, **54**, 11169–11186.
- 25 G. Kresse and J. Furthmüller, *Comput. Mater. Sci.*, 1996, **6**, 15–50.
- 26 X. Zhang, G. Zhang, T. Jia, Y. Guo, Z. Zeng and H. Q. Lin, *Phys. Lett. Sect. A Gen. At. Solid State Phys.*, 2011, **375**, 2456–2459.
- 27 A. Togo and I. Tanaka, *Scr. Mater.*, 2015, **108**, 1–5.
- 28 S. Curtarolo, W. Setyawan, G. L. W. Hart, M. Jahnatek, R. V. Chepurskii, R. H. Taylor, S. Wang, J. Xue, K. Yang, O. Levy, M. J. Mehl, H. T. Stokes, D. O. Demchenko and D. Morgan, *Comput. Mater. Sci.*, 2012, **58**, 218–226.
- 29 R. D. Shannon, *Acta Crystallogr. Sect. A*, 1976, **32**, 751–767.
- 30 J. Lorenzana, A. Grzelak, V. Struzhkin, D. Kurzydłowski, M. Derzsi, W. Grochala and P. Barone, *Chem. Commun.*, 2018, **54**, 10252–10255.

Electronic supplementary information

Crystal structure, lattice dynamics and superexchange in MAgF_3 1D antiferromagnets ($\text{M} = \text{K}, \text{Rb}, \text{Cs}$) and $\text{Rb}_3\text{Ag}_2\text{F}_7$ Ruddlesden-Popper phase

Kacper Koteras,^{1*} Jakub Gawraczyński,¹ Gašper Tavčar,² Zoran Mazej,² Wojciech Grochala¹

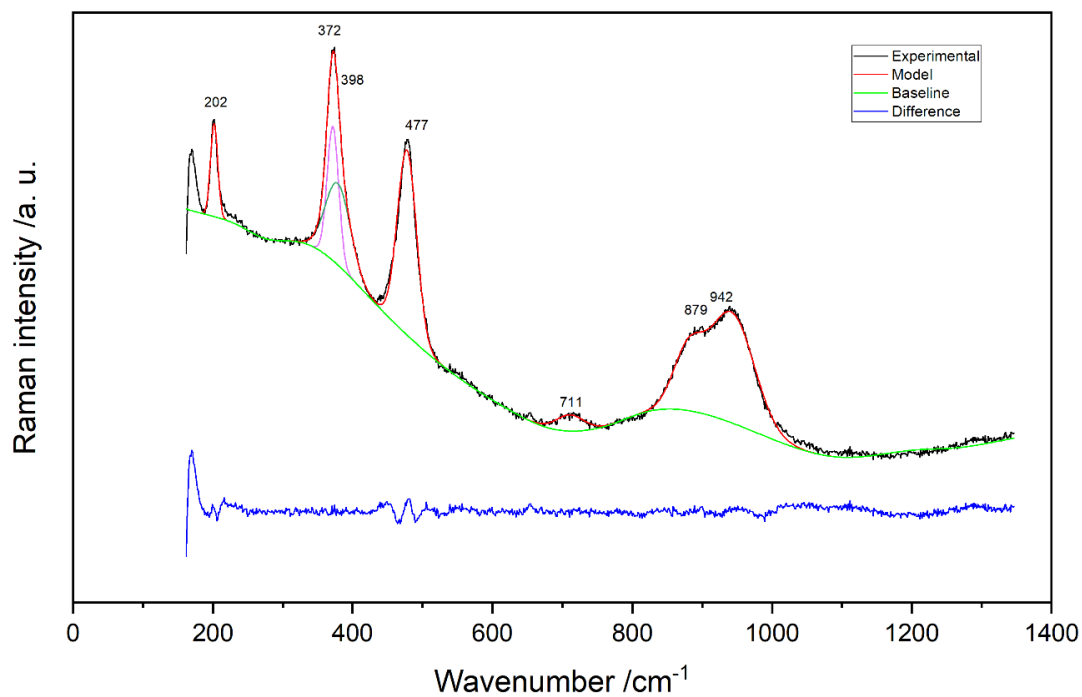


Figure S1. Deconvoluted Raman spectrum of CsAgF_3 .

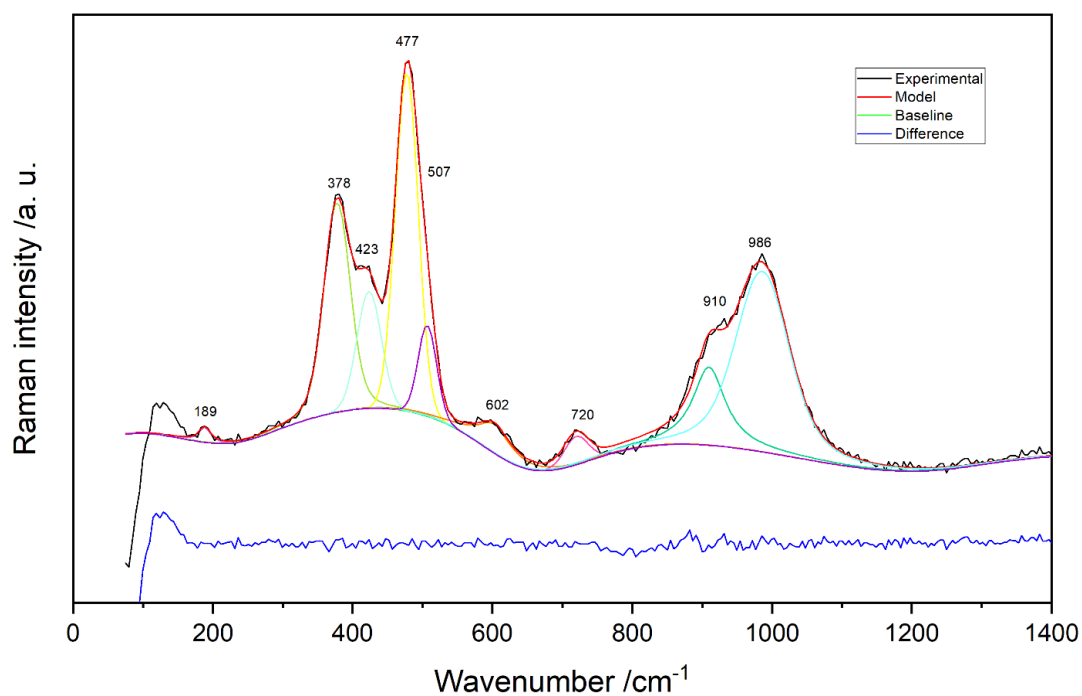


Figure S2. Deconvoluted Raman spectrum of RbAgF_3 .

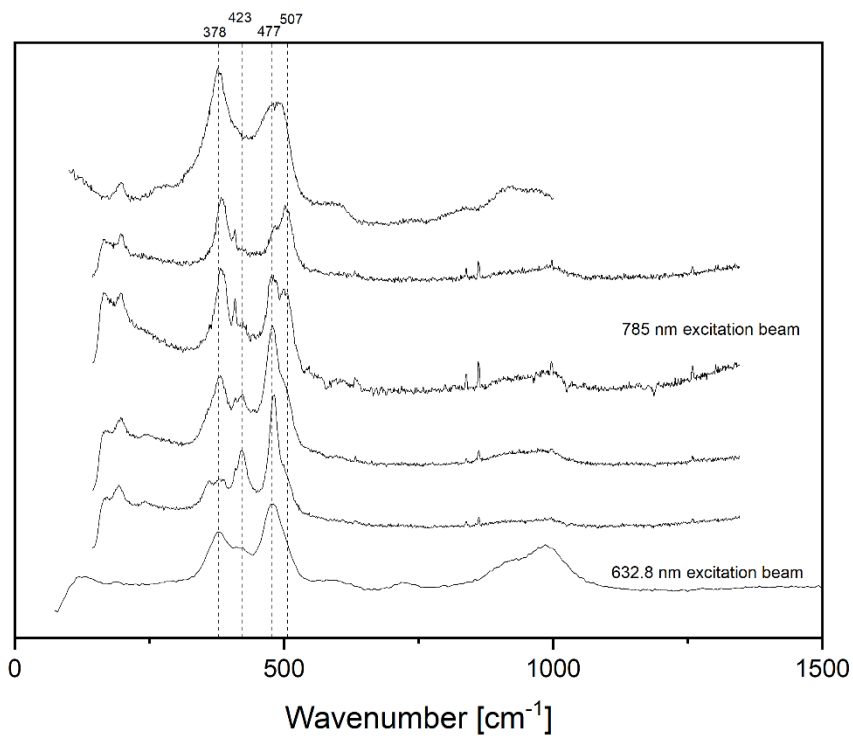


Figure S3. Different Raman spectra collected for of RbAgF₃.

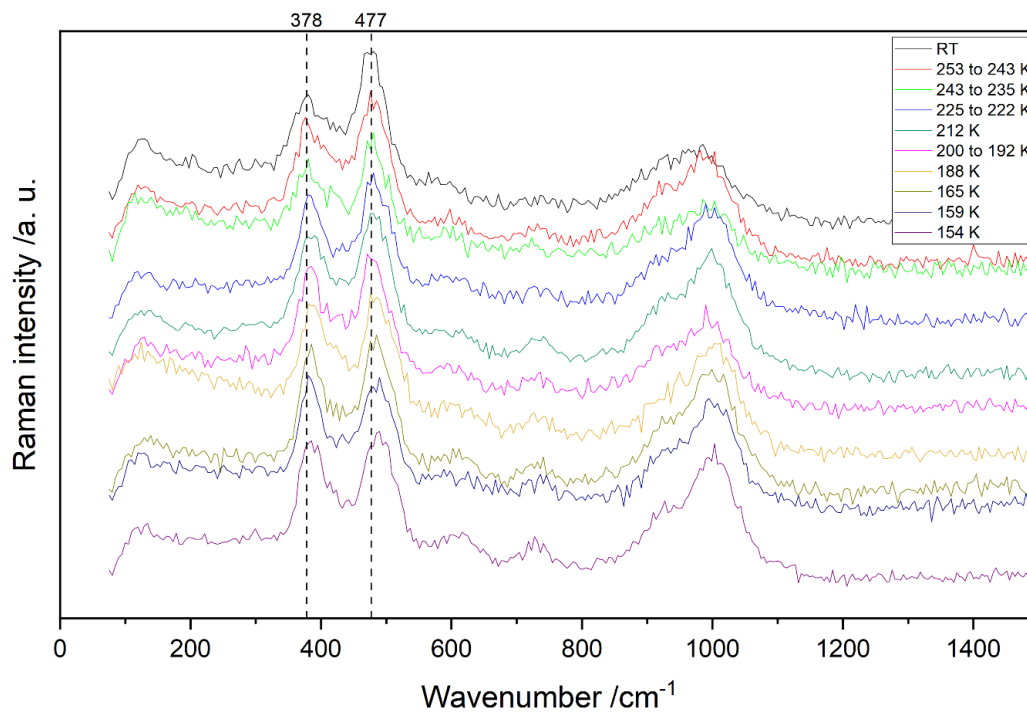


Figure S4. Full set of Raman spectra at low temperature for RbAgF₃.

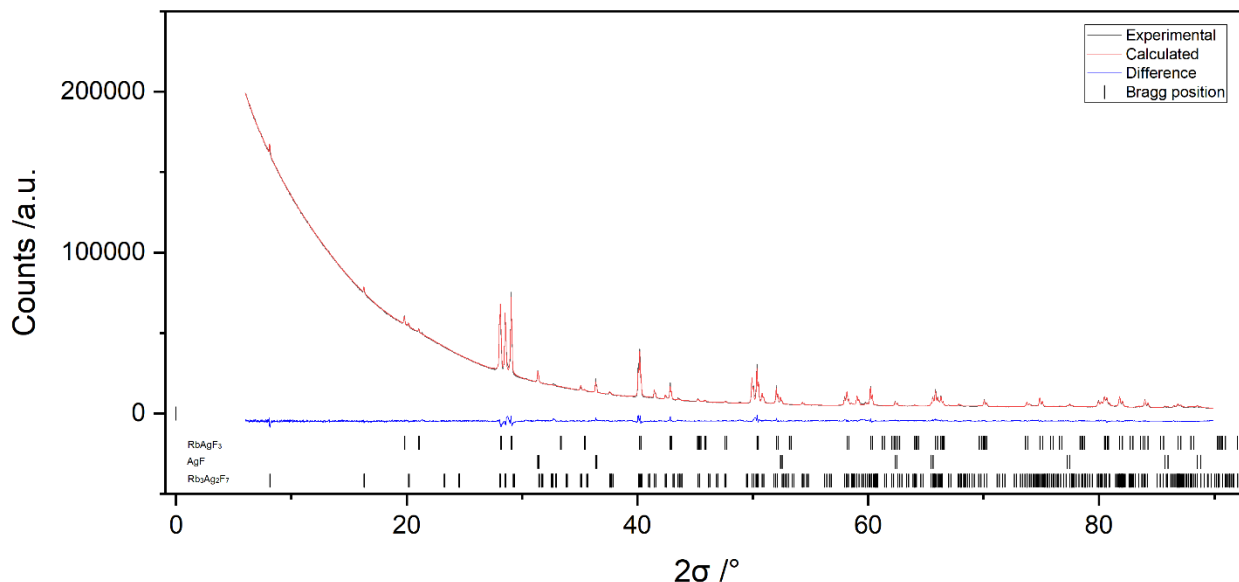


Figure S5. X-ray diffraction pattern of RbAgF₃ sample containing novel Rb₃Ag₂F₇ phase and the results of the Rietveld refinement. Bottom part shows simulated Bragg positions for each present phase (from top to bottom: RbAgF₃, AgF and Rb₃Ag₂F₇).

Table S1. Crystallographic data for RbAgF₃.

Formula	RbAgF ₃
Colour	brown
Space group	<i>I4/mcm</i> (No. 140)
<i>Z</i>	4
<i>V</i> /Å ³	338.991(6)
<i>a</i> /Å	6.33855(6)
<i>b</i> /Å	6.33855(6)
<i>c</i> /Å	8.43740(11)
α /°	90
β /°	90
γ /°	90
Positions	Rb1 0.00000 0.00000 0.25000 Ag1 0.00000 0.50000 0.00000 F1 0.00000 0.50000 0.25000 F2 0.240(4) 0.740(4) 0.00000
Reliability factors	Not corrected for background (all data) R _P = 0.84 % R _{wp} = 1.78 % Corrected for background (all data) cR _P = 27.86 % cR _{wp} = 15.16 % R Bragg factor (this phase) R _{Bragg} = 9.53 %
Atomic distances /Å	Ag–F (apical) 2.10935(3) Ag–F (equatorial) 2.33(3) 2.15(3)

Table S2. Theoretically calculated modes.

RbAgF ₃ <i>Pnma</i> (HSE06)		RbAgF ₃ <i>I4/mcm</i> (HSE06)		CsAgF ₃ <i>I4/mcm</i> (HSE06)	
B _{2u}	471	A _{2u}	484	E _u	450
A _u	470	B _{2g}	472	B _{2g}	449
B _{3g}	467	E _u	467	A _{2u}	449
B _{1u}	464	A _{1g}	381	A _{1g}	370
B _{3u}	464	B _{2g}	312	B _{2g}	302
A _u	462	B _{1u}	233	B _{1u}	227
B _{2u}	461	E _g	184	A _{2u}	193
B _{2g}	449	A _{2u}	183	E _u	186
B _{1g}	414	E _u	181	E _g	186
A _g	380	E _u	159	E _u	162
B _{1g}	365	A _{2g}	144	B _{1u}	155
B _{3g}	303	B _{1u}	139	A _{2g}	150
B _{3u}	271	E _u	124	E _u	118
B _{1u}	240	A _{2g}	69	B _{1g}	95
B _{3u}	205	A _{2u}	67	E _g	88
A _g	201	E _u	66	A _{2u}	72
B _{2g}	200	E _g	65	E _u	72
B _{1u}	199	E _g	26	A _{2g}	65
B _{2u}	186	A _{2u}	-1	E _g	56
B _{2g}	182	E _u	-2	A _{2u}	-5
B _{1u}	175	B _{1g}	-39	E _u	-5
B _{3u}	174				
A _u	174				
A _u	164				
B _{2u}	162				
B _{3u}	161				
B _{1u}	157				
B _{3g}	153				
B _{2u}	146				
A _u	146				
B _{1g}	139				
B _{1u}	139				
B _{3g}	134				
B _{3u}	134				
B _{3u}	129				
B _{2g}	125				
B _{1u}	118				
A _g	98				
A _g	87				
B _{1g}	86				
B _{1u}	82				
A _g	78				
B _{3g}	77				
A _u	76				
B _{3u}	76				
B _{2u}	74				
B _{2g}	73				
B _{2u}	71				
A _g	69				
B _{3u}	68				
B _{1u}	65				
A _u	64				
B _{2g}	60				
B _{1g}	50				
A _u	49				
B _{2g}	34				
A _g	33				
B _{2u}	-1				
B _{1u}	-1				
B _{3u}	-2				

Cif files of structures used in lattice dynamics calculations

RbAgF₃ *Pnma* (HSE06)

```
data_findsym-output
_audit_creation_method FINDSYM

_cell_length_a 6.2633870000
_cell_length_b 8.3574660000
_cell_length_c 6.3444310000
_cell_angle_alpha 90.0000000000
_cell_angle_beta 90.0000000000
_cell_angle_gamma 90.0000000000
_cell_volume 332.1058636297

_symmetry_space_group_name_H-M "P 21/n 21/m 21/a"
_symmetry_Int_Tables_number 62
_space_group.reference_setting '062:-P 2ac 2n'
_space_group.transform_Pp_abc a,b,c;0,0,0

loop_
_space_group_symop_id
_space_group_symop_operation_xyz
1 x,y,z
2 x+1/2,-y+1/2,-z+1/2
3 -x,y+1/2,-z
4 -x+1/2,-y,z+1/2
5 -x,-y,-z
6 -x+1/2,y+1/2,z+1/2
7 x,-y+1/2,z
8 x+1/2,y,-z+1/2

loop_
_atom_site_label
_atom_site_type_symbol
_atom_site_symmetry_multiplicity
_atom_site_Wyckoff_label
_atom_site_fract_x
_atom_site_fract_y
_atom_site_fract_z
_atom_site_occupancy
_atom_site_fract_symmform
Ag1 Ag 4 a 0.00000 0.00000 0.00000 1.00000 0,0,0
Rb1 Rb 4 c 0.00381 0.25000 0.49913 1.00000 Dx,0,Dz
F1 F 4 c 0.49600 0.25000 0.45836 1.00000 Dx,0,Dz
F2 F 8 d 0.26645 -0.02118 0.27814 1.00000 Dx,Dy,Dz
```

RbAgF₃ *I4/mcm* (HSE06)

```
data_findsym-output
_audit_creation_method FINDSYM

_cell_length_a 6.2963000000
_cell_length_b 6.2963000000
_cell_length_c 8.4031760000
_cell_angle_alpha 90.0000000000
_cell_angle_beta 90.0000000000
_cell_angle_gamma 90.0000000000
_cell_volume 333.1304144144

_symmetry_space_group_name_H-M "I 4/m 2/c 2/m"
_symmetry_Int_Tables_number 140
_space_group.reference_setting '140:-I 4 2c'
_space_group.transform_Pp_abc a,b,c;0,0,0

loop_
_space_group_symop_id
_space_group_symop_operation_xyz
1 x,y,z
2 x,-y,-z+1/2
```

3 -x,y,-z+1/2
 4 -x,-y,z
 5 -y,-x,-z+1/2
 6 -y,x,z
 7 y,-x,z
 8 y,x,-z+1/2
 9 -x,-y,-z
 10 -x,y,z+1/2
 11 x,-y,z+1/2
 12 x,y,-z
 13 y,x,z+1/2
 14 y,-x,-z
 15 -y,x,-z
 16 -y,-x,z+1/2
 17 x+1/2,y+1/2,z+1/2
 18 x+1/2,-y+1/2,-z
 19 -x+1/2,y+1/2,-z
 20 -x+1/2,-y+1/2,z+1/2
 21 -y+1/2,-x+1/2,-z
 22 -y+1/2,x+1/2,z+1/2
 23 y+1/2,-x+1/2,z+1/2
 24 y+1/2,x+1/2,-z
 25 -x+1/2,-y+1/2,-z+1/2
 26 -x+1/2,y+1/2,z
 27 x+1/2,-y+1/2,z
 28 x+1/2,y+1/2,-z+1/2
 29 y+1/2,x+1/2,z
 30 y+1/2,-x+1/2,-z+1/2
 31 -y+1/2,x+1/2,-z+1/2
 32 -y+1/2,-x+1/2,z

loop_
 _atom_site_label
 _atom_site_type_symbol
 _atom_site_symmetry_multiplicity
 _atom_site_Wyckoff_label
 _atom_site_fract_x
 _atom_site_fract_y
 _atom_site_fract_z
 _atom_site_occupancy
 _atom_site_fract_symmform
 Ag1 Ag 4 d 0.00000 0.50000 0.00000 1.00000 0,0,0
 Rb1 Rb 4 a 0.00000 0.00000 0.25000 1.00000 0,0,0
 F1 F 4 b 0.00000 0.50000 0.25000 1.00000 0,0,0
 F2 F 8 h 0.22870 0.72870 0.00000 1.00000 Dx,Dx,0

CsAgF₃ *I4/mcm* (HSE06)

data_findsym-output
 _audit_creation_method FINDSYM

 _cell_length_a 6.4411370000
 _cell_length_b 6.4411370000
 _cell_length_c 8.4690630000
 _cell_angle_alpha 90.0000000000
 _cell_angle_beta 90.0000000000
 _cell_angle_gamma 90.0000000000
 _cell_volume 351.3665678866

 _symmetry_space_group_name_H-M "I 4/m 2/c 2/m"
 _symmetry_Int_Tables_number 140
 _space_group.reference_setting 'I 4 2c'
 _space_group.transform_Pp_abc a,b,c;0,0,0

loop_
 _space_group_symop_id
 _space_group_symop_operation_xyz
 1 x,y,z
 2 x,-y,-z+1/2
 3 -x,y,-z+1/2
 4 -x,-y,z
 5 -y,-x,-z+1/2

6 -y,x,z
 7 y,-x,z
 8 y,x,-z+1/2
 9 -x,-y,-z
 10 -x,y,z+1/2
 11 x,-y,z+1/2
 12 x,y,-z
 13 y,x,z+1/2
 14 y,-x,-z
 15 -y,x,-z
 16 -y,-x,z+1/2
 17 x+1/2,y+1/2,z+1/2
 18 x+1/2,-y+1/2,-z
 19 -x+1/2,y+1/2,-z
 20 -x+1/2,-y+1/2,z+1/2
 21 -y+1/2,-x+1/2,-z
 22 -y+1/2,x+1/2,z+1/2
 23 y+1/2,-x+1/2,z+1/2
 24 y+1/2,x+1/2,-z
 25 -x+1/2,-y+1/2,-z+1/2
 26 -x+1/2,y+1/2,z
 27 x+1/2,-y+1/2,z
 28 x+1/2,y+1/2,-z+1/2
 29 y+1/2,x+1/2,z
 30 y+1/2,-x+1/2,-z+1/2
 31 -y+1/2,x+1/2,-z+1/2
 32 -y+1/2,-x+1/2,z

loop_
 _atom_site_label
 _atom_site_type_symbol
 _atom_site_symmetry_multiplicity
 _atom_site_Wyckoff_label
 _atom_site_fract_x
 _atom_site_fract_y
 _atom_site_fract_z
 _atom_site_occupancy
 _atom_site_fract_symmform
 Ag1 Ag 4 d 0.00000 0.50000 0.00000 1.00000 0,0,0
 Cs1 Cs 4 a 0.00000 0.00000 0.25000 1.00000 0,0,0
 F1 F 4 b 0.00000 0.50000 0.25000 1.00000 0,0,0
 F2 F 8 h 0.22363 0.72363 0.00000 1.00000 Dx,Dx,0

Rb₃Ag₂F₇ *Cmca* (GGA+U)

data_findsym-output
 _audit_creation_method FINDSYM

 _cell_length_a 21.6756500000
 _cell_length_b 6.2943600000
 _cell_length_c 6.2937100000
 _cell_angle_alpha 90.0000000000
 _cell_angle_beta 90.0000000000
 _cell_angle_gamma 90.0000000000
 _cell_volume 858.6781972783

 _symmetry_space_group_name_H-M "C 2/m 2/c 21/a"
 _symmetry_Int_Tables_number 64
 _space_group.reference_setting '064:-C 2ac 2'
 _space_group.transform_Pp_abc a,b,c;0,0,0

 loop_
 _space_group_symop_id
 _space_group_symop_operation_xyz
 1 x,y,z
 2 x,-y,-z
 3 -x+1/2,y,-z+1/2
 4 -x+1/2,-y,z+1/2
 5 -x,-y,-z
 6 -x,y,z

7 $x+1/2, -y, z+1/2$
8 $x+1/2, y, -z+1/2$
9 $x+1/2, y+1/2, z$
10 $x+1/2, -y+1/2, -z$
11 $-x, y+1/2, -z+1/2$
12 $-x, -y+1/2, z+1/2$
13 $-x+1/2, -y+1/2, -z$
14 $-x+1/2, y+1/2, z$
15 $x, -y+1/2, z+1/2$
16 $x, y+1/2, -z+1/2$

loop_

_atom_site_label

_atom_site_type_symbol

_atom_site_symmetry_multiplicity

_atom_site_Wyckoff_label

_atom_site_fract_x

_atom_site_fract_y

_atom_site_fract_z

_atom_site_occupancy

_atom_site_fract_symmform

Ag1 Ag 8 d 0.40284 0.00000 0.00000 1.00000 Dx,0,0

Rb1 Rb 8 d 0.18085 0.00000 0.00000 1.00000 Dx,0,0

Rb2 Rb 4 a 0.00000 0.00000 0.00000 1.00000 0,0,0

F1 F 8 d 0.30625 0.00000 0.00000 1.00000 Dx,0,0

F2 F 4 b 0.50000 0.00000 0.00000 1.00000 0,0,0

F3 F 16 g 0.09527 0.26940 0.23077 1.00000 Dx,Dy,Dz